ADVANCED MATERIALS

Supporting Information

for *Adv. Mater.*, DOI 10.1002/adma.202301339

Large Anomalous Nernst Effects at Room Temperature in Fe_3Pt Thin films

Minghang Li, Hanqi Pi, Yunchi Zhao, Ting Lin, Qinghua Zhang, Xinzhe Hu, Changmin Xiong, Zhiyong Qiu, Lichen Wang, Ying Zhang, Jianwang Cai, Wuming Liu, Jirong Sun, Fengxia Hu, Lin Gu, Hongming Weng, Quansheng Wu*, Shouguo Wang*, Yunzhong Chen* and Baogen Shen*

Supporting Information

Large anomalous Nernst effects at room temperature in Fe_3Pt thin films

Minghang Li,[1,2†] Hanqi Pi,[1,2†] Yunchi Zhao,[1,3] Ting Lin,[1,2] Qinghua Zhang,[1] Xinzhe Hu,[1] Changmin Xiong,[3] Zhiyong Qiu,[5] Lichen Wang[6], Ying Zhang,[1,2] Jianwang Cai,[1,2] Wuming Liu,[1,2] Jirong Sun,[1,2] Fengxia Hu,[1,2] Lin Gu,[1] Hongming Weng,[1,2] Quansheng Wu[1,2*], Shouguo Wang,[4*] Yunzhong Chen,[1,2*] Baogen Shen[1,2,6,7]*

[1]*Beijing National Laboratory of Condensed Matter Physics and Institute of Physics, Chinese Academy of Sciences, Beijing 100190, China*

[2]*School of Physical Sciences, University of Chinese Academy of Sciences, Beijing 100049, China;*

[3]*Department of Physics, Beijing Normal University, Beijing 100875, China;*

[4]*School of Materials Science and Engineering, Anhui University, Hefei 230601, China*

[5]*School of Material Science and Engineering, Dalian University of Technology, Dalian 116024, China*

[6]*Ningbo Institute of Materials Technology & Engineering, Chinese Academy of Sciences, Ningbo, Zhejiang, 315201, China*

[7]*Ganjiang Innovation Academy, Chinese Academy of Sciences, Ganzhou, Jiangxi, 341000, China*

*Email: yzchen@iphy.ac.cn; quansheng.wu@iphy.ac.cn; cmxiong@bnu.edu.cn; sgwang@ahu.edu.cn

†Equal contribution.

Contents

1. Crystalline structure by XRD

Figure S1 shows the X-ray diffraction (XRD) profile for the samples deposited at different temperatures T_s from 600℃ to 900℃. The (001) diffraction peak was detected when the deposition temperature was 600℃ and above, indicating the transform from a *A*1 disordered phase to $L1_0/L1_2$ ordered phase. As temperature increases from 600℃ to 900℃, the intensity of (001) peak was enhanced, indicating the increase of the crystalline content of the samples. The calculated lattice parameters by XRD with the assumption of $a=b$ were provided in the Table S1. The slight smaller c than the bulk lattice constant value ($a=b=c$=3.74Å) is due to the tensile strain which makes lattice structure elongated in the a-b plane and compressed in c-axis when grown on the MgO substrate (a =4.21 Å).

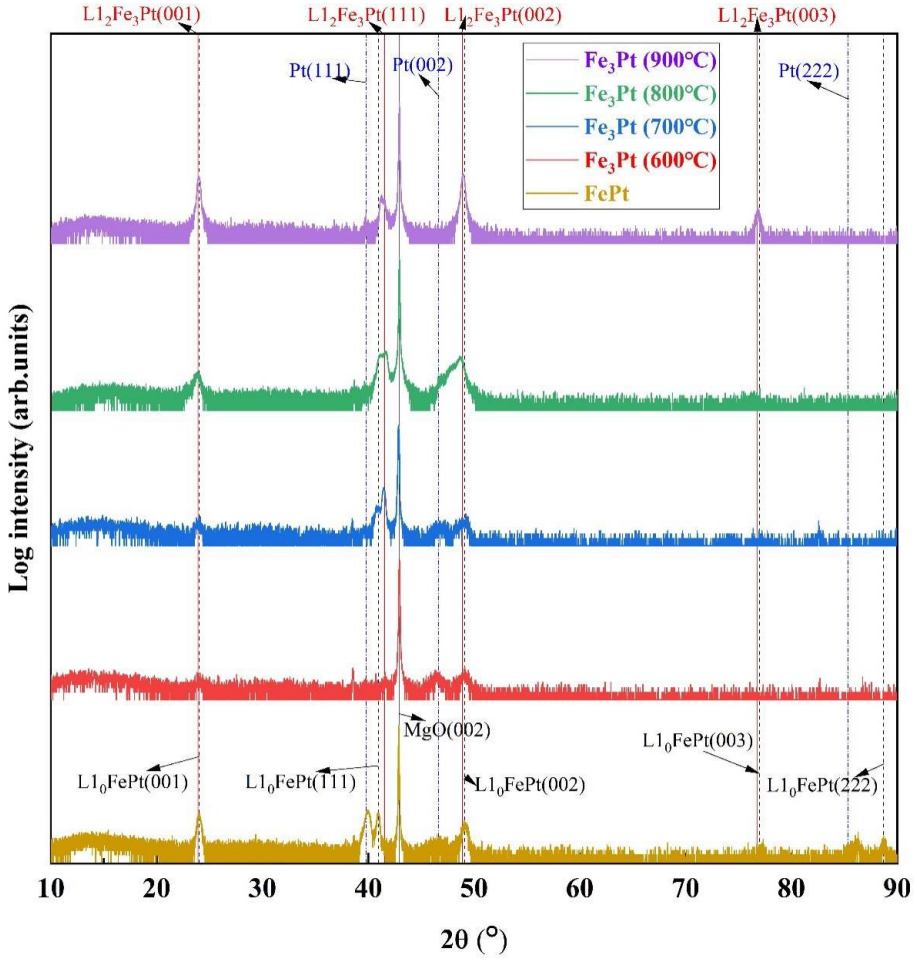

Figure S1. XRD pattern for the $Fe_{75}Pt_{25}$ compound films prepared at different deposition temperatures and the FePt film prepared at 500 ℃.

Table S1. Lattice parameters of the $Fe_{75}Pt_{25}$ compound films as a function of T_s determined by XRD.

Deposition temperature T_s (℃)	**Lattice Parameter** (Å)		
	a	***b***	***c***
600	-	-	3.711
700	3.765	3.765	3.717
800	3.791	3.791	3.741
900	3.815	3.815	3.719

2. Transmission Electron Microscopy (TEM)

High resolution TEM measurements were also performed on two samples grown at 700℃ and 900℃, as shown in Fig.S2. The lattice parameters of selected regions were also shown. By comparing the lattice parameter with those of the bulk materials (Table S2), we can identify that: for the film grown at 700℃ where the diffusion is limited, clear phase boundaries could be observed. The upper part above the buffer layer is $L1_2$ Fe_3Pt phase as expected. Notably, an interlayer with mostly $L1_0$ FePt where Fe layers and Pt layers stacked alternately of bright and dark is observed between the $L1_2$ Fe_3Pt and the Pt buffer layer (the red region in Figure S2a). Additionally, the lattice parameters measured from the brightest region (marked as green in Figure S2a) coincide well with those of bulk Pt (Table S2). Thus the intermixing part is composed of $L1_0$ FePt, Pt and Cr-Pt compounds, although it remains challenging to determine the exact ratio of each component. For films grown at 900℃ as shown in Figure S2b, the buffer layer is hardly detectable. The selected (red and green) regions both show stacked patterns of alternately bright and dark, which indicates that most of the film is dominated by a $L1_0$ phase due to significant diffusion.

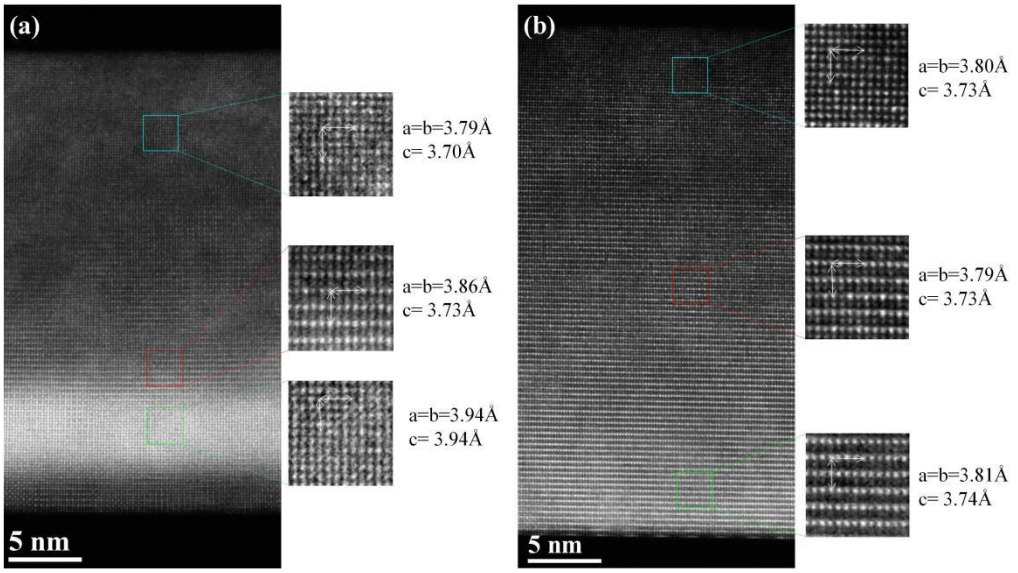

Figure S2. TEM patterns of Fe_3Pt prepared at 700℃ **a)** and 900℃ **b)**. Regions with different colors were extracted to calculate lattice parameter. The measured length is indicated by a white arrow.

Table S2. lattice parameters of bulk Fe-Pt compounds.

Materials	**Lattice Parameters (Å)**		
	a	***b***	***c***
Fe_3Pt (bulk)	3.74	3.74	3.74
FePt (bulk)	3.86	3.86	3.77
Pt (bulk)	3.94	3.94	3.94

The Energy Dispersive X-ray (EDX) microanalysis were also performed on the sample grown at 700℃ for both the buffer layer and the Fe_3Pt regions, and the calculated composition percentages of Fe and Pt atoms For the two regions are presented in Figure S3. The atomic ratio Fe:Pt of the Fe_3Pt film region (red) is 2.24, and the buffer layer region (blue) is 0.63. So there is indeed iron intermixing occurred during the high temperature deposition.

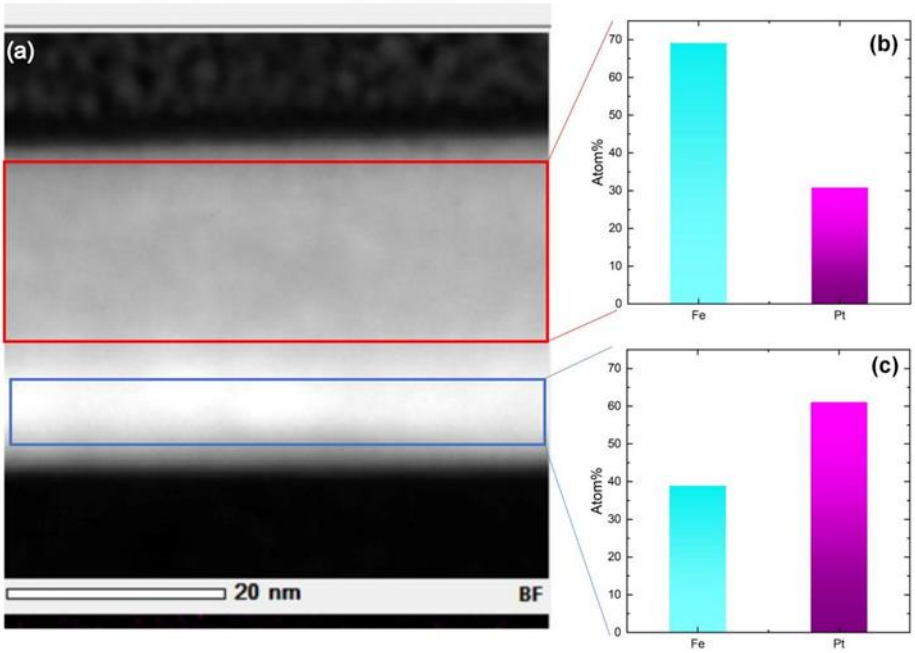

Figure S3. a) Low-magnification HAADF image of the Fe_3Pt films grown at 700℃. Atomic percentage of Fe and Pt atoms in the red region **b)** and blue region **c)**.

3. Magnetic properties

The magnetic properties were measured by SQUID VSM. The out-of-plane magnetization hysteresis loops of Fe_3Pt films at 300 K prepared at different substrate temperatures (T_s=600℃-900℃) are shown in Figure S4a. As summarized in Figure S4b, the saturation magnetization (M_s) increases from 6.1 μ_B/f.u. for T_s= 600℃ to 7.3 μ_B/f.u. for T_s= 900℃, and the coercivity (H_c) decreases from 800 Oe to 30 Oe (Figure S4b), indicating the phase transition from the disordered phase to the ordered phase[1].

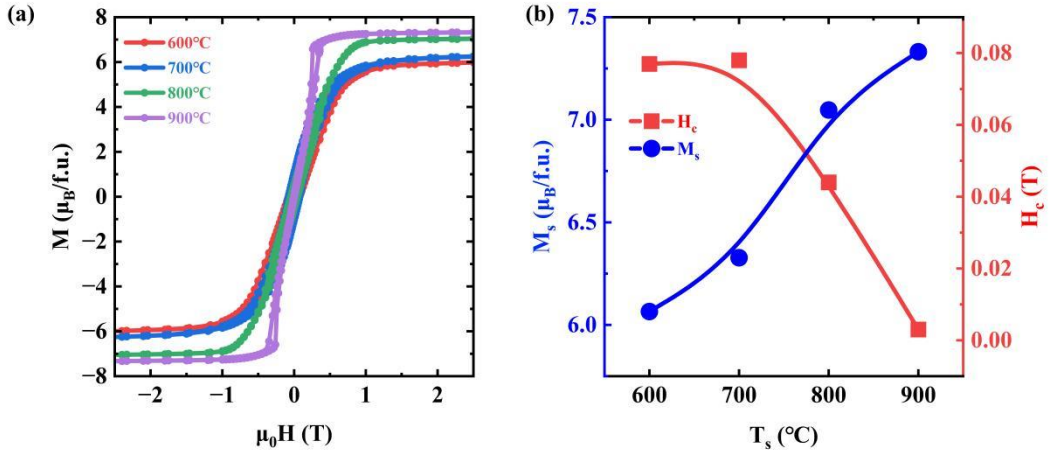

Figure S4. a) Out-of-plane magnetization hysteresis loops at 300 K for the Fe_3Pt films prepared at substrate temperatures of T_s=600℃-900℃. **b)** The saturation magnetization (M_s) and coercivity (H_c) as a function of with the preparation temperature (T_s).

To explore the magnetic anisotropy of the Fe_3Pt and FePt films. Magnetic field ($\mu_0 H$) dependence of magnetization (M) was also measured under magnetic field which was applied parallel to the plane and perpendicular to the plane. As is shown in Figure S5, the Fe_3Pt exhibit smaller magnetic anisotropy than FePt due to its nearly symmetric lattice structure as illustrated in Figure 1c.

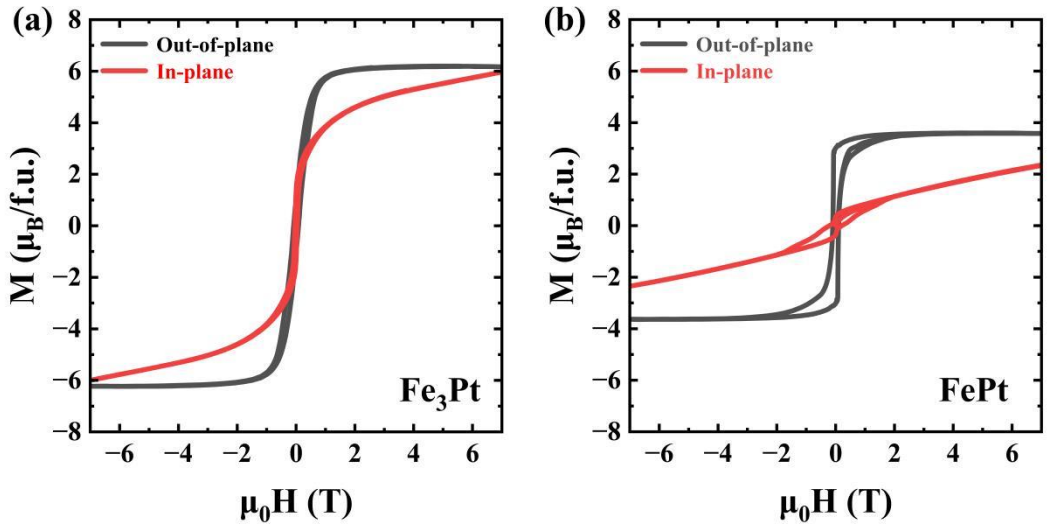

Figure S5. Magnetocrystalline anisotropy of Fe_3Pt and FePt
Out-of-plane (black) and In-plane (red) magnetic hysteresis loops at 300K for **a)** Fe_3Pt and **b)** FePt.

4.Thermal Transport Measurement

For thermal transport measurement, the samples were patterned into a Hall bar structure with a width of 1.0 mm and a length of 3.8 mm by using photolithography and Ar-ion milling, as shown in Figure S6a. The thermal signal T_{hot} and T_{cold} can be detected at two plug-in thermometer shoes in the PPMS Thermal Transport Option (TTO) which were connected to the copper lead attached to the sample through a high thermal conductivity adhesive ((Figure S6b). The anomalous Nernst signal was measured at room temperature by using the TTO at magnetic fields ranging from -2 T to 2 T, which were applied perpendicular to the film plane. The ANE thermopower, S_{yx}, defined as the ANE voltage standardized by the width of Hall bar (w) and applied temperature gradient ∇T i.e. $S_{yx} = (V_y/w)/(-\nabla_x T)$. The temperature gradient was measured by two thermometer shoes in TTO, which was calculated to be 0.31~0.51 K mm^{-1}. The thermal conductivity of all samples was measured during the thermal transport measurements, and the value ranged from 56.5 W K^{-1}m^{-1} to 61.5 W K^{-1}m^{-1}. This is because that the thermal resistance of the MgO substrate is much lower than that of films, the thermal conductivity (κ) of the MgO ($\kappa \approx 60$ WK^{-1}m^{-1}) substrate becomes the main contribution[2-4].

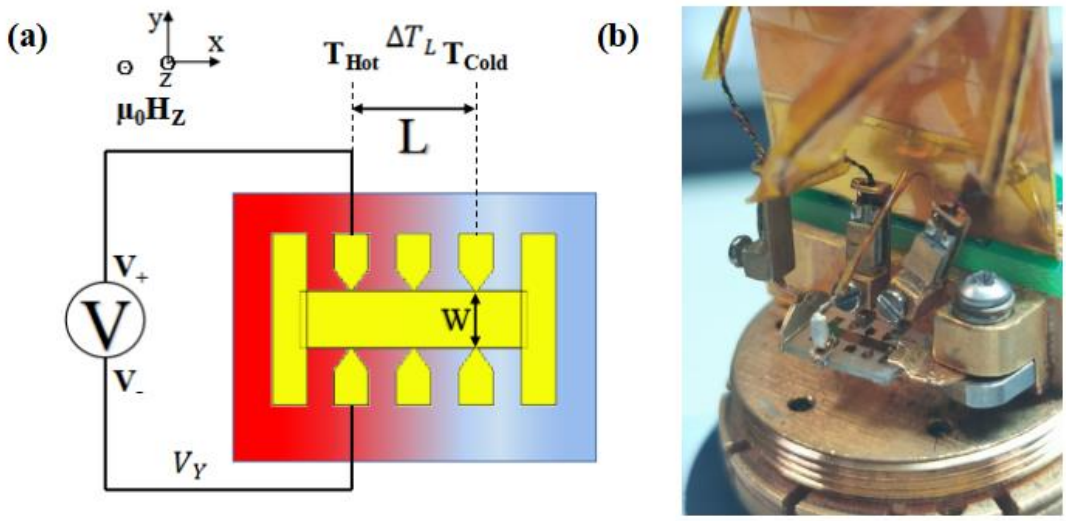

Figure S6. a) Schematic diagram of Hall bar pattern in samples. **b)** Image of TTO measurement.

Figure S7a shows the magnetic field ($\mu_0 H$**)** dependence of ANE thermopower S_{yx} for Fe_3Pt films prepared at different temperatures. Most samples exhibit a S_{yx} larger than that of the FePt (~0.5 μV K^{-1}), and the sample deposited at 700℃ show the highest S_{yx}~2 μV K^{-1}, which is one magnitude larger than α-Fe (~0.2 μV K^{-1})[5] and almost four times larger than the FePt. Figure S7b shows Magnetic field ($\mu_0 H$**)** dependence of Hall resistivity (ρ_{yx}) for the Fe_3Pt films prepared at different temperatures. With the increase of the T_s, ρ_{yx} increases from 1.7μΩ cm to 3.7μΩ cm. The different behavior in the T_s dependence between S_{yx} and ρ_{yx} further indicates that the intrinsic ANE is determined by the Berry curvature near the Fermi surface, whereas the anomalous Hall effect is obtained by an integration of the Berry curvature for all of the occupied bands.

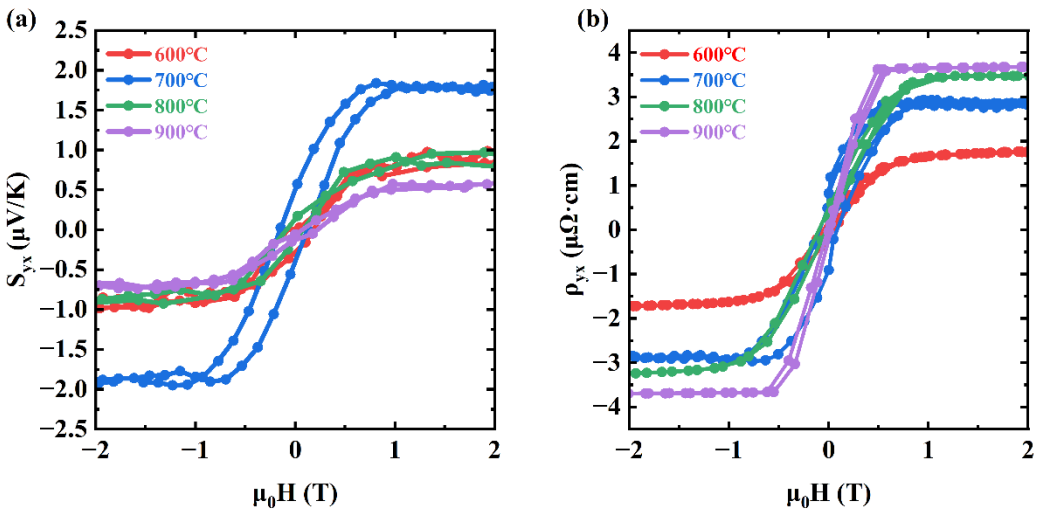

Figure S7. a) Magnetic field ($\mu_0 H$**)** dependence of ANE thermopower S_{yx} measured in Fe_3Pt films which were prepared at different temperatures. **b)** Magnetic field ($\mu_0 H$**)** dependence of Hall resistivity (ρ_{yx}) for the Fe_3Pt films prepared at different temperatures.

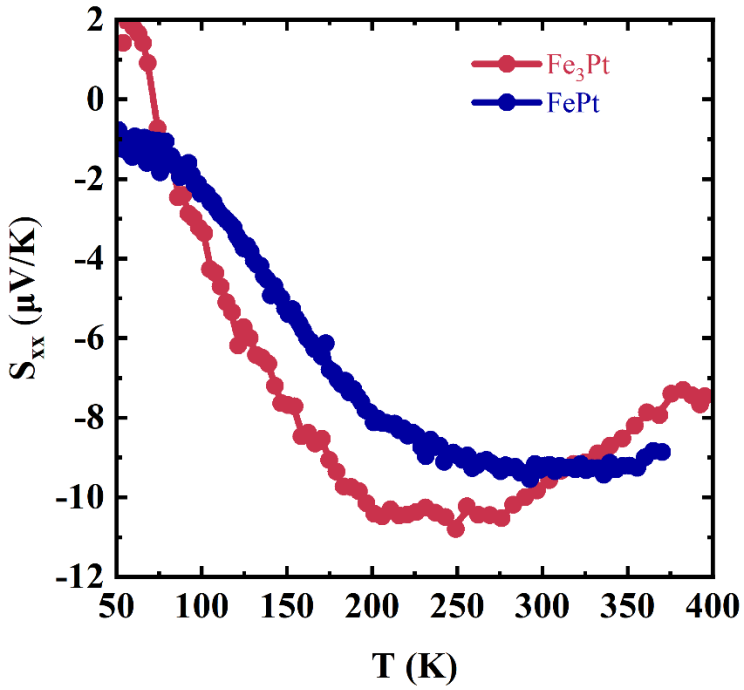

Figure S8. Temperature dependence (T) of Seebeck coefficient (S_{xx}) in Fe_3Pt (red) and FePt (blue) from 50 K to 400 K.

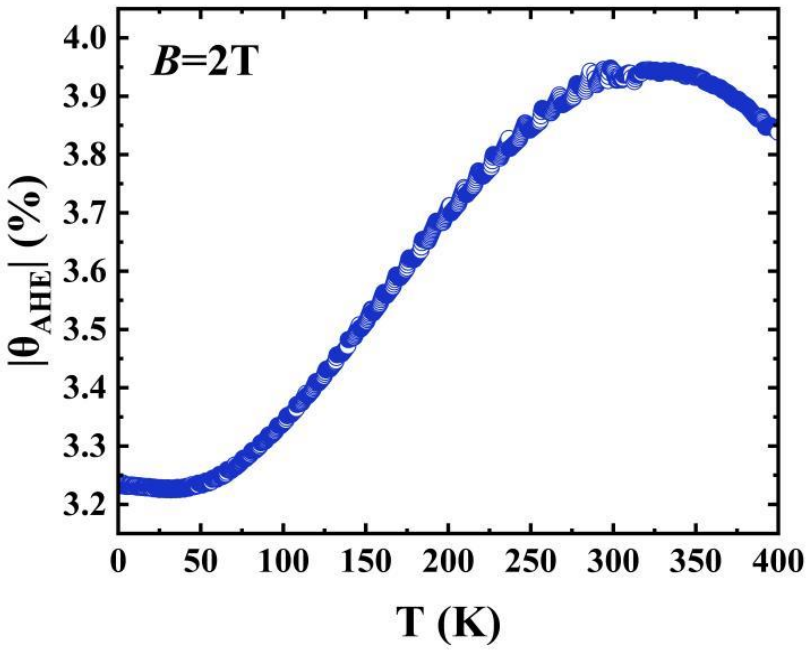

Figure S9. Temperature dependence of anomalous Hall angle ($|\theta_{AHE}| = \rho_{yx}/\rho_{xx}$) in Fe_3Pt thin film.

Table S3. Comparison of transverse thermoelectric conductivity, $|\alpha_{yx}|$ in different Fe-Pt-based alloy films at room temperature.

Formula	$\|\alpha_{yx}\|$ (300K) (A $K^{-1}m^{-1}$)
Fe_3Pt	3.4
FePt	1.5
FePt[6]	0.9
FePt[7]	0.8
FePt(int)[7]	0.8

.

5. DFT Calculation

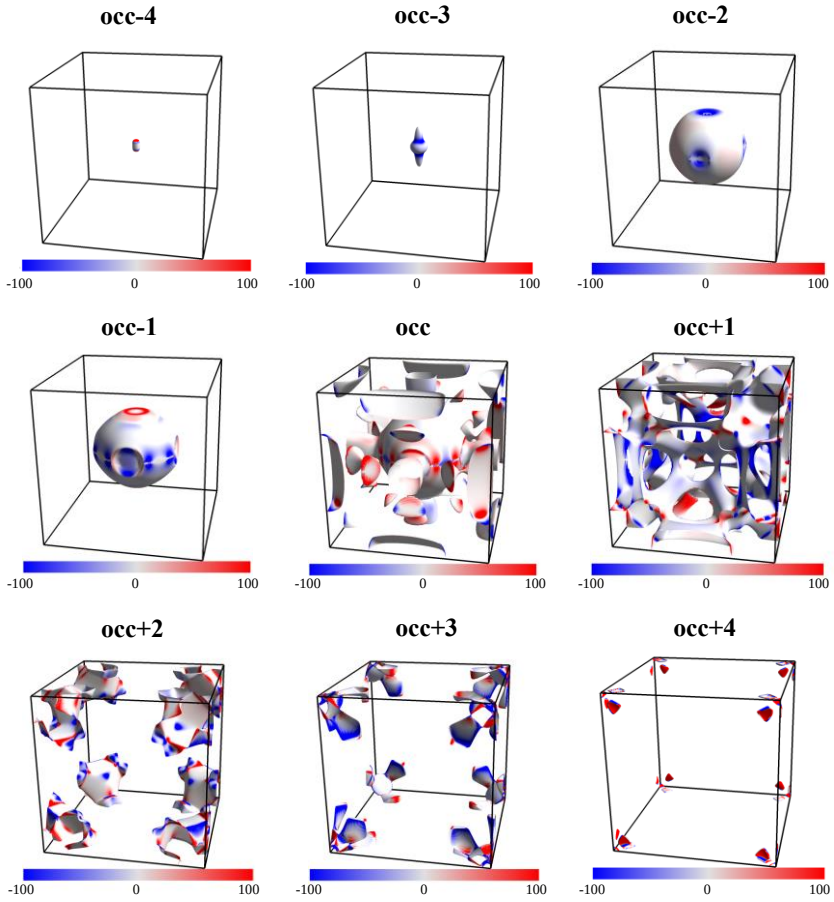

Figure S10. Berry curvature $\Omega_{xy}(\boldsymbol{k})$ on Fermi surfaces in the BZ with the contributions from relevant energy bands illustrated separately. Occ denotes the highest occupied band.

When the spin and orbit degree of freedom are decoupled, all the symmetry operations in *Pm-3m* (No.221) space group are preserved. The degenerated states on R(Γ-R) in Figure 5a denoted by green arrows(circles) belong to the three-dimensional(two-dimensional) irreducible representations R4±(LD3) of the little group *3m*(*m-3m*), which were computed by *irvsp* package.[8] We adapt the definition for the irreducible representations by Bilbao Crystallographic Server.[9] With SOC included, however, there are only one-sixth of symmetry operations in *Pm-3m* (No.221) space group preserved and the ferromagnetic $L1_2$-Fe_3Pt belongs to *P4/mm'm'* (No.123.345) magnetic space group. As the new little groups of R and Γ-R only contain one-dimensional core presentations, the degeneracy of bands is lifted as shown in Figure 5 b. Therefore, the introduction of SOC leads to a series of small energy gaps and large

Berry curvature in the BZ. Because the intrinsic ANE α_{yx} is determined by Berry curvature Ω_{xy} near the Fermi energy, we calculate the $\Omega_{xy}(k)$ on the Fermi surface and the band structure with SOC. As seen from Figure 5 b-c and Figure S10, $\Omega_{xy}(k)$ is distributed throughout the BZ, especially around R, which results in the large intrinsic ANE of $L1_2$-Fe_3Pt.

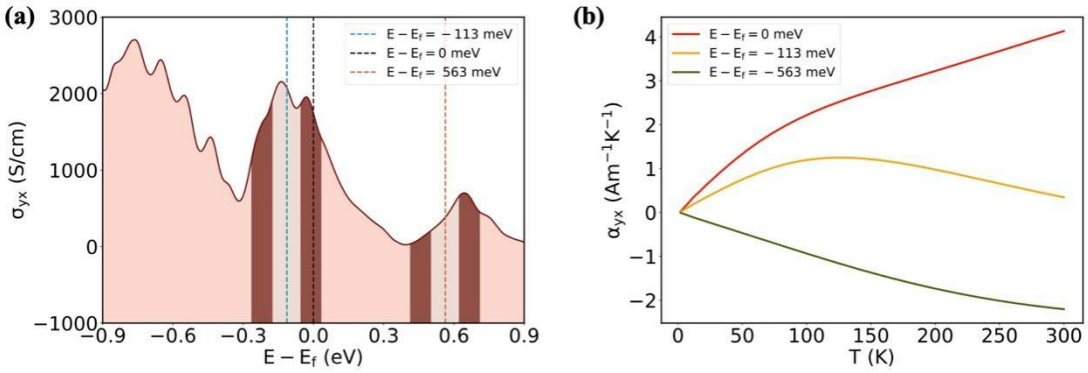

Figure S11. a) Calculated energy-dependent $\sigma_{yx}(\mu)$. There are two sections composed of the brown region and the beige region centering at -113 meV and 563 meV. The beige region is the contribution range of $\sigma_{yx}(\varepsilon)$ at 100 K which covers 100 meV. The brown regions on two sides of the beige regions have a range of 172 meV, resulting from the increasing temperature from 100 K to 300 K. **b)** Calculated temperature-dependent $\alpha_{yx}(T)$ at different chemical potentials.

As seen from Equation (1), the intrinsic ANE α_{yx} can be regarded as the contribution from σ_{yx} near the chemical potential weighted by $w(\varepsilon,T) = \frac{1}{e}\frac{\partial f(\varepsilon)}{\partial \varepsilon}\frac{(\varepsilon-\mu)}{T}$. We define the main contribution range of $\sigma_{yx}(\mu)$ at different temperatures as the energy region where $\frac{\partial f(\varepsilon)}{\partial \varepsilon}|_T < 10^{-3}$. As w is an odd function with respect to μ (μ=E-E_F), $|\alpha_{yx}|$ increases with temperature if σ_{yx} on one side of chemical potential μ is always larger than the other side in the contribution range. As shown in Figure S11a, we denote the contribution range (100 meV) at 100 K with beige color and represent the increment of the contribution range (172 meV) from 100 K to 300 K with brown color. Within the beige and brown region centering at μ=563 meV, $\sigma_{yx}(\varepsilon)$ below 563 meV is smaller than the above $\sigma_{yx}(\varepsilon)$ at the same distance away from 563 meV, leading to the increase of $|\alpha_{yx}|$ from 2 K to 300 K. It also explains the temperature-dependence of α_{yx} at the charge neutral point. However, for chemical potential set at -113 meV, $\sigma_{yx}(\varepsilon)$ below μ dominates

the contribution to α_{yx} from 2 K to 100 K, while the $\sigma_{yx}(\varepsilon)$ above μ contributed mostly from 100 K to 300 K. As the contribution effects of $\sigma_{yx}(\varepsilon)$ at two sides of the chemical potential are opposite, α_{yx} at μ=-113 meV increases from 2 K to 100 K and then decreases as shown in Figure S11b.

We also added the calculation results of $L1_0$FePt, including the electronic structure, anomalous Hall conductivity, and transverse thermoelectric conductivity, as shown in Figure S12. Our analysis shows that the anomalous Hall conductivity in $L1_0$FePt has a smaller variation near the Fermi level (~849 S/(cm·eV)) compared to Fe_3Pt (~9147 S/(cm·eV)). According to the Mott relation, this results in a much smaller transverse thermoelectric conductivity in FePt. Moreover, The experiment value α_{yx} at room temperature of FePt in our work (~1.5A·m^{-1}K^{-1}) is smaller than Fe_3Pt (~3.4A·m^{-1}K^{-1}) (Table S3), so the large ANE in Fe_3Pt is attributed to the larger intrinsic α_{yx} through theory and experiments.

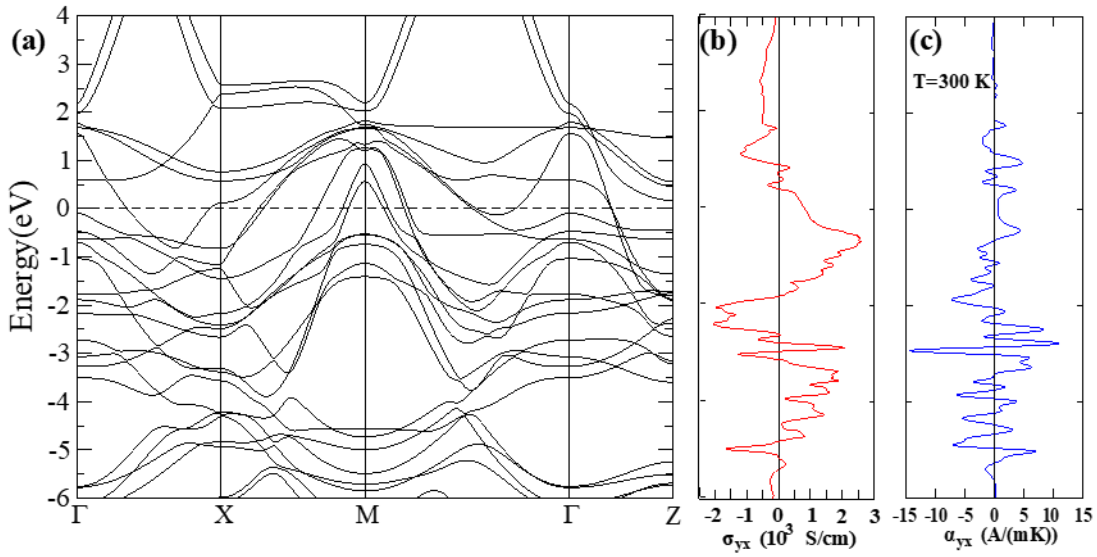

Figure S12. (a) The band structure with SOC of $L1_0$FePt. (b) Calculated energy-dependent σ_{yx}. (c) Calculated energy-dependent transverse thermoelectric conductivity, α_{yx}, at 300 K.

[1] S. N. Hsiao, S. K. Chen, S. H. Liu, H. Y. Lee, *J. Appl. Phys.* **2012**, 111, 07A313.
[2] N. de Koker, *Phys. Rev. Lett.* **2009**, 103, 125902.
[3] S. Stackhouse, L. Stixrude, B. B. Karki, *Phys. Rev. Lett.* **2010**, 104, 208501.
[4] A. Giri, S. H. Wee, S. Jain, O. Hellwig, P. E. Hopkins, *Scientific reports* **2016**, 6, 1.
[5] X. Li, L. Xu, L. Ding, J. Wang, M. Shen, X. Lu, K. Behnia, *Phys. Rev. Lett*. **2017**, 119, 056601.
[6] K. Hasegawa, M. Mizuguchi, Y. Sakuraba, T. Kamada, T. Kojima, T. Kubota, K. Takanashi, *Appl. Phys. Lett.* **2015**, 106, 252405.
[7] Z. Shi, S. J. Xu, L. Ma, S. M. Zhou, G. Y. Guo, *Physical Review Applied* **2020**, 13, 054044.
[8] J. Gao, Q. Wu, C. Persson, Z. Wang, *Computer Physics Communications* **2021**, 261, 107760.
[10] L. Elcoro, B. Bradlyn, Z. Wang, M. G. Vergniory, J. Cano, C. Felser, M. I. Aroyo, *Journal of Applied Crystallography* **2017**, 50, 1457.